Elliptic pillars based metasurface for elastic waves focusing in a plate

*Original*
Elliptic pillars based metasurface for elastic waves focusing in a plate / Carpentier, L., Gueddida, A., Lévêque, C., Alcorta-Galvan, R., Croënne, C., Miniaci, M., Djafari-Rouhani, B., Pennec, Y.. - In: APL MATERIALS. - ISSN 2166-532X. - 12:4(2024).

*Publisher:*
AIP Publishing

*Published*
DOI:

APL Materials

RESEARCH ARTICLE | APRIL 01 2024

# Elliptic pillars based metasurface for elastic waves focusing in a plate

**Special Collection:** New Frontiers in Acoustic and Elastic Metamaterials and Metasurfaces

L. Carpentier; A. Gueddida ; G. Lévêque ; R. Alcorta-Galvan ; C. Croënne ; M. Miniaci ;
B. Djafari-Rouhani ; Y. Pennec ✉

Check for updates

*APL Mater.* 12, 041102 (2024)
https://doi.org/10.1063/5.0193284

View Online

Export Citation

## Articles You May Be Interested In

Topological elastic interface states in hyperuniform pillared metabeams

*APL Mater.* (January 2024)

Local resonances in phononic crystals and in random arrangements of pillars on a surface

*J. Appl. Phys.* (September 2013)

Subwavelength waveguiding of surface phonons in pillars-based phononic crystal

*AIP Advances* (November 2014)

AIP Publishing

**APL Materials** ARTICLE pubs.aip.org/aip/apm

# Elliptic pillars based metasurface for elastic waves focusing in a plate

Cite as: APL Mater. 12, 041102 (2024); doi: 10.1063/5.0193284
Submitted: 21 December 2023 • Accepted: 14 March 2024 •
Published Online: 1 April 2024

L. Carpentier,[1] A. Gueddida,[1] G. Lévêque,[1] R. Alcorta-Galvan,[2] C. Croënne,[2] M. Miniaci,[2] B. Djafari-Rouhani,[1] and Y. Pennec[1,a)]

## AFFILIATIONS

[1] Institut d'Electronique, de Microélectronique et de Nanotechnologies, UMR CNRS 8520, Université de Lille, 59650 Villeneuve d'Ascq, France
[2] Univ. Lille, CNRS, Centrale Lille, Junia, University Polytechnique Hauts-de-France, UMR 8520 - IEMN - Institut d'Electronique de Microélectronique et de Nanotechnologie, F-59000 Lille, France

**Note:** This paper is part of the Special Topic on New Frontiers in Acoustic and Elastic Metamaterials and Metasurfaces.
[a)] **Author to whom correspondence should be addressed:** yan.pennec@univ-lille.fr

## ABSTRACT

In this paper, the ability of a metasurface made of resonant elliptical pillars to focus flexural Lamb waves in the sub-wavelength regime is investigated. We report on the influence of the ellipticity parameter on the local resonances of the pillars, in particular the monopolar compressional and dipolar bending modes that are responsible for the desired focusing effect. We also discuss how the transmission through a line of pillars reveals these modes when the orientation of the pillars is changed with respect to the incident wave. Both the resonances can be superimposed for a particular choice of the ellipticity parameter, allowing a phase shift of $2\pi$ in the transmission coefficient for an incident antisymmetric Lamb wave, which is a necessary condition for the design of the metasurface. Finally, a gradient design for the pillar ellipticity is investigated, and its capacity to choose the focusing directionality of the transmitted wave at different targeted points is demonstrated.

## I. INTRODUCTION

Metasurfaces are metamaterials of sub-wavelength thickness made of a large number of discrete scatterers that locally and collectively modify the scattering properties of an incident wave. Initially developed in the domain of electromagnetic waves,[1] the working principle of metasurfaces has since been extended to many other fields of wave physics, such as optics,[2–4] acoustics,[5–9] and wave propagation in elastic media.[10–14] The specific design of the metasurfaces allows for unusual and particularly appealing properties if compared to those of ordinary homogeneous materials, such as the ability to deviate,[15–18] focus,[19,20] guide, or filter[21,22] waves. In particular, sub-wavelength filtering in precise frequency ranges[23–25] or controlling the transmission direction of a plane wave (either by deflecting it according to a desired refraction angle[26] or by focusing it at different targeted points) have been shown as very promising applications in terms of waves propagating within a half-space or plate-like structures. To achieve such functionalities, a recent study[27] proposed the design of a sub-wavelength metasurface consisting of a row of cylindrical pillars for robust deep sub-wavelength focusing and imaging of elastic waves on a plate of thickness $e = 145$ $\mu$m. The sub-wavelength pillar diameter was fixed to $d = 120$ $\mu$m, while their heights were varied around a specific value of $h = 240$ $\mu$m. Such parameters allowed for the superposition of the second bending and the first compressional resonances, which was indeed required to allow the transmission phase shift at resonance to reach $2\pi$ (which cannot be achieved when the two resonances are separated). A gradual change in the height of the pillars around this reference value allowed us to tune the phase shift over a $2\pi$ range while maintaining a high level of transmission. However, fabricating such a metasurface with variable pillar heights at the microscale, while feasible, requires a technological step for each height variation, regardless of the lithography process employed. Consequently, such fabrication is time-consuming and costly and could potentially impact the reproducibility of the metasurface. Consequently, we propose a different approach based on the design of pillars of elliptical shape characterized by a constant height. In this case, the ellipticity of the scatterers is the key parameter for the superposition of a bending mode and a compressional mode, i.e., the two involved resonances to achieve the required phase shift. The design of the proposed metasurface consists of an array of resonant pillars of different ellipticity parameters, allowing it to realize a gradient phase shift fully covering a $2\pi$ range.

The paper is organized as follows: Sec. II presents the different resonance modes of an individual pillar on a substrate based on the analysis of the dispersion curves and the deformation maps. The focus is on the comparison between the properties of cylindrical pillars and those with an elliptical geometry. It is shown that the breaking of rotational invariance considerably modifies the nature of some modes and their resonant frequencies. In Sec. III, the transmission curves of a row of identical pillars to determine the resonance modes that are most sensitive to the ellipticity of the pillars are investigated with the aim of determining the conditions under which the two resonant modes can be superimposed (thus producing the $2\pi$ phase shift required for the architecture of the metasurface). In this transmission study, the effects of tilting the major axis of the pillar by an angle $\varphi$ with respect to the incident wave are also presented. This tilt reveals additional resonance modes compared to the case of pillars oriented along the direction of propagation of the incident wave, but without affecting the major goal of the metasurface. Finally, in Sec. IV, we will apply these results to the design of different metasurface geometries, which will enable an incident Lamb wave of type $A_0$ to be focused at different points on the plate.

## II. BAND DIAGRAM AND DISPLACEMENT FIELDS OF A PERIODIC ARRANGEMENT OF PILLARS

Figure 1(a) reports a schematic representation of the unit cell geometry adopted for the calculation of the dispersion diagrams [Figs. 1(b) and 1(c)]. The dispersion diagrams of the elliptic shaped pillars [Fig. 1(c)] are compared with those of an equivalent cylindrical pillar structure [Fig. 1(b)]. The dispersion diagrams are calculated via the commercial finite element software Comsol Multiphysics©. The solid mechanics module is exploited under the following boundary conditions: Floquet–Bloch periodicity is applied along the $x$- and $y$-directions [refer to Fig. 1(a)], whereas free surface conditions are set on the top and bottom surfaces of the plate and the boundaries of the pillars. In all subsequent simulations, the following constant geometrical parameters are adopted: a thickness of the plate $e = 145$ µm, a height of the pillars $h = 240$ µm, a small

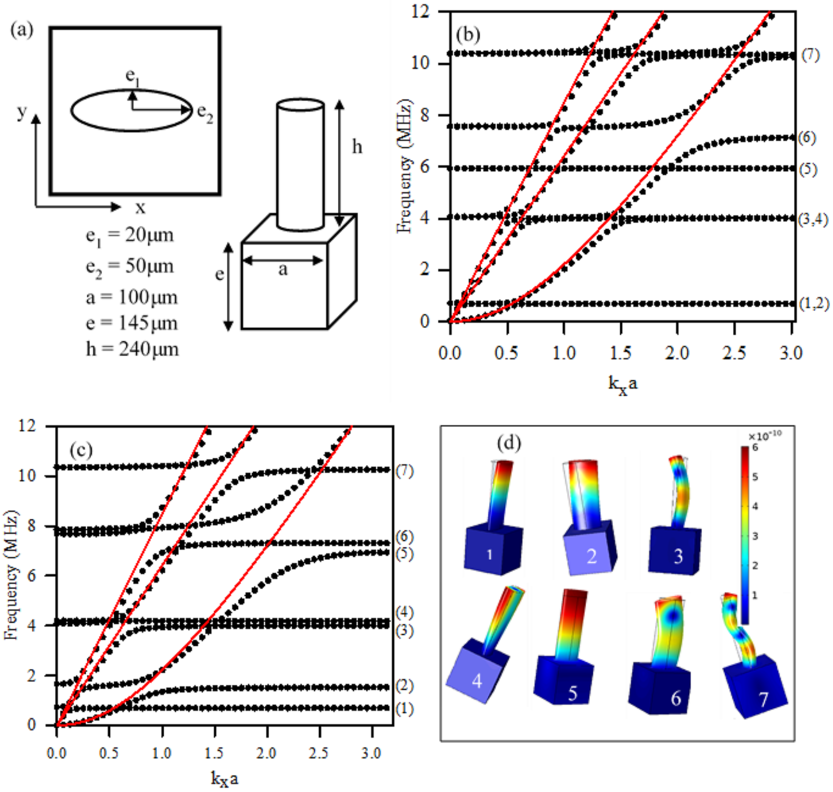

**FIG. 1.** (a) Geometry and parameters used for the calculation of the dispersion curves of (b) dispersion curves for cylindrical pillars with $e_1 = e_2 = 20$ $\mu$m; the red solid lines correspond to the $A_0$, $SH_0$, and $S_0$ Lamb waves of the plate without pillars. (c) Elliptic pillars with $e_1 = 20$ µm and $e_2 = 50$ $\mu$m. (d) Displacement field maps of the resonant modes of the elliptic pillar. All the modes are given at the same reduced wave vector value, $k_x.a = \pi$. They correspond to the three first bending modes (1, 2) (3, 4) (7), the torsional mode (5), and the compressional mode (6).

axis value of the elliptic pillars $e_1 = 20$ µm, and a lattice parameter $a = 100$ µm. The ellipticity parameter $e_2$ will be used as the adjustable parameter. All these geometrical parameters are recalled in Fig. 1(a). Silicon is chosen as the material for the entire structure. The crystallographic axes [100], [010], and [001] of the face-centered cubic unit cell are aligned to the ($x$, $y$, $z$) directions in Fig. 1(a). The components of the elastic tensor are taken as $C_{11} = 16.57 \times 10^{10}$ Nm$^{-2}$, $C_{12} = 6.39 \times 10^{10}$ Nm$^{-2}$, $C_{44} = 7.962 \times 10^{10}$ Nm$^{-2}$, and the density of silicon is $\rho = 2331$ kg m$^{-3}$. Figures 1(b) and 1(c) show the dispersion curves in the 0–12 MHz frequency range for cylindrical-shaped pillars (i.e., $e_2 = e_1 = 20$ µm) and for elliptical-shape pillars with an ellipticity parameter $e_2 = 50$ µm, respectively. Solid red curves correspond to the three first Lamb modes of the plate in the absence of pillars. To label the different modes of the pillars in the rest of the paper, we number the resonant modes of the cylindrical pillars in ascending order of frequency in Fig. 1(b). Then, the modes of the elliptic pillars presenting similar mode shapes can be equally labeled in Fig. 1(c). In the cylindrical case [Fig. 1(b)], the first two sets of doubly degenerated low frequency modes 1–2 and 3–4 are the first and second order bending modes of the pillar along the $x$ and $y$ directions, occurring at $f = 0.65$ MHz and $f = 3.99$ MHz, respectively. At higher frequencies (in order of increasing frequency), the first torsion mode (5), the compressional mode (6), and the degenerate third-order bending mode (7) appear. The degeneracy of the bending modes is lifted for the elliptic pillar due to the loss of radial symmetry. Since $e_1$ is kept constant, two bending modes with displacements along the $y$-direction are noticeable at the same frequencies as for the cylindrical pillar, and the other two bending modes, with displacements along the $x$-direction are found around 0.65 and 3.99 MHz, respectively. Let us note that due to the increase in $e_2$, these other two modes with displacements along the $x$-direction are upshifted in frequency. As expected, this shift gets more pronounced as the difference between $e_1$ and $e_2$ increases. This phenomenon is also observed for higher order bending modes (second order bending modes 3 and 4, as well as third order bending mode 7). The torsional mode (5) is now present at lower frequencies ($f = 4.17$ MHz) because the moment of inertia of the pillar is increased due to a higher mass that is also distributed further from the center of inertia, hence lowering the frequency. The shape of the pillar also likely modifies the effective rotational stiffness, making the evolution of the mode with respect to $e_2$ more complex. The frequency of the compressional mode (6) is hardly modified since the deformation of the pillar is only in the out-of-plane direction, thus unaffected by the in-plane profile of the pillar.

## III. ELASTIC WAVE TRANSMISSION FOR A LINE OF IDENTICAL PILLARS

In this section, we investigate the effect of the resonant modes of the pillars on the transmission (amplitude and phase) of the $A_0$ Lamb mode propagating across a line of identical elliptic pillars, of height $h$, arranged on a plate of thickness $e$, with pillar centers positioned every $a = 100$ µm in the direction perpendicular to the impinging wave front. For these calculations, we have considered the effect of the two following geometrical parameters, namely, the ellipticity parameter $e_2$ and the orientation of the pillars with respect to the direction of an incident elastic wave ($x$-direction) indicated by angle $\varphi$ (see the schematic representation of the structure in Fig. 2). Two different values of $\varphi$ are investigated as follows: $\varphi = 0°$ and $\varphi = 45°$. The method used to compute the resonances is as follows: an oscillating force is applied, normal to the surface of the plate, along a line (AB) parallel to the crystallographic direction (010) of the silicon (referred to as the $y$-axis in the following), and the resulting normal displacements are recorded as a function of frequency on a line (CD) located on the other hand of the pillar row. An infinite line of identical pillars is obtained by applying Floquet–Bloch Periodic Boundary Conditions (PBCs.) on the boundaries perpendicular to the $y$-axis, and Perfect Matched Layers (PMLs.) located at each end of the plate are used to avoid any reflection from the boundaries.

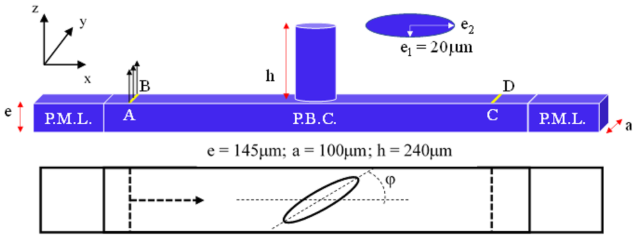

**FIG. 2.** Model used for finite element calculations of the transmission coefficient through a periodic line of identical pillars. A time-periodic vertical force is applied along (AB). PMLs are placed at both ends of the plate, and periodic boundary conditions (PBCs) are applied on the lateral sides to simulate an infinite line of pillars. The amplitude of displacement $u_z$ as a function of frequency is monitored along (CD).

We first compute $u_z$ on the line (CD) against the frequency for a row of elliptical pillars whose major axis, designed by $e_2$, is oriented in the direction of propagation of the incident wave, i.e., $\varphi = 0°$, as a function of $e_2$ ranging between 20 and 70 µm by steps of 10 µm. Since the $A_0$ mode is mostly polarized in the $z$-direction, we define the transmission as the displacement component $u_z$ at the line (CD) when the pillars are modeled and normalized by $u_z$ at the line (CD) when the pillars are removed in the simulation. The transmission is shown in Fig. 3 for different values of $e_2$. The presence of dips in the transmission curves reflects the excitation of pillar modes by the incident wave. In the explored frequency range (0–12 MHz), the first four resonance modes are identifiable through more or less sharp dips in the transmission curve and can be unambiguously ascribed to the three first bending modes (2), (4), and (7), and to the first compressional mode (6) (see Fig. 1). We can note that mode (7) is only observed for $e_2 = 20$ µm, as this mode shifts rapidly to frequencies outside of the range of interest for larger values of $e_2$. Second, no signature corresponding to the torsional mode (5) is observable. Actually, due to the symmetry of the incident wave, this mode cannot be excited by the incident Lamb wave. Modes (2) and (6) are rather insensitive to variations of the parameter $e_2$ defining the elliptic shape of the pillar, whereas the second order bending mode (4) rapidly shifts toward high frequencies as $e_2$ increases. Finally, modes (4) and (6) end up overlapping at the frequency of 7.48 MHz when the value of $e_2$ reaches 50 µm.

When the pillars are oriented with an angle $\varphi = 45°$ with respect to the incident wave, all the modes observed on the dispersion curves inFig. 1(c) have their signature on the transmission curve. Compared to the $\varphi = 0°$ case, in addition to the separation of bending modes

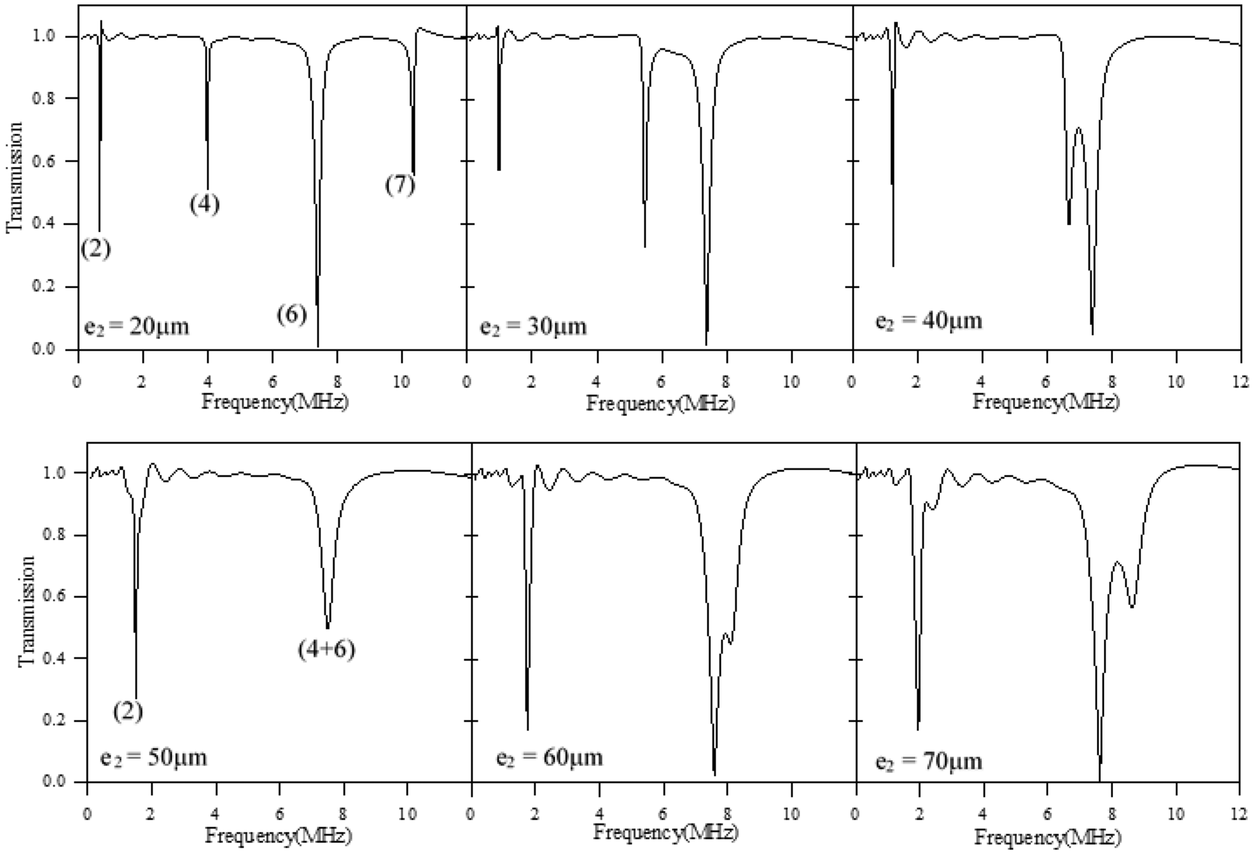

**FIG. 3.** Transmission through a line of elliptical pillars whose major axis $e_2$ is parallel to the direction of propagation of the incident wave, $\varphi = 0°$. Each curve is associated with a different value of $e_2$, ranging from $e_2 = 20$ µm, corresponding to the cylindrical pillar, to $e_2 = 70$ µm, in steps of 10 µm.

(1, 2) and (3, 4) in the $e_1$ and $e_2$ directions, we now observe the occurrence of extremely sharp dips associated with torsional modes labeled 5 and 8. These torsional modes are only visible on the transmission curves for $e_2 \geq 60$ µm. Indeed, below $e_2 = 60$ µm, the first order torsional mode, is overlapped with the second order bending mode (3), which is much broader in the transmission spectrum. The second order torsional mode referred to as (8), lies above the frequency window studied as far as $e_2 < 60$ µm since this mode shifts to higher frequencies as $e_2$ decreases. To better highlight the signature of the torsional modes, we report in Fig. 5 a zoom of the red ($e = 60$ $\mu$m) and blue ($e = 70$ $\mu$m) boxes depicted in Fig. 4. Figure 5(a) reports the two fundamental torsional modes, while Fig. 5(b) shows the third-order bending mode (7) and second-order torsional mode (8).

It is worth noting that the first-order torsional mode (5) evolves in the same way as both the bending modes along the $e_2$ axis and the compressional one, namely, they shift toward higher frequencies as $e_2$ increases. In contrast, an opposite behavior is observed for the second order torsional mode (8). Furthermore, these two torsional modes show up on the transmission curve as extremely sharp peaks, reflecting very high-quality factors. The resonant frequencies of the various modes observed between 0 and 12 MHz are plotted as a function of $e_2$ in Fig. 6 for the two angles $\varphi = 0°$ [Fig. 6(a)] and $\varphi = 45°$ [Fig. 6(b)].

Varying the orientation of the pillars with respect to the incident wave has almost no influence on the frequencies of modes (2), (4), and (6). It reveals, in addition to the torsional modes (5 and 8), bending ones along the $y$ direction (modes 1, 3, and 7), whose resonant frequencies are independent of $e_2$. This is understandable since these additional modes only depend on the $e_1$ value, which remains constant here. We also note that the dips of transmission are deeper for $\varphi = 0°$. As shown in Fig. 6(a), bending modes (2) and (4) present a high sensitivity to the value of $e_2$, with a particularly rapid evolution of the second order mode (4). Therefore, this mode crosses the evolution of the compressional mode (6) for $e_2 = 50$ µm. This salient feature makes it possible to use elliptic pillars to create a gradient metasurface for plane-wave focusing. Indeed, it is well known that, whereas a variation of the phase around a resonance generally spans a range of $\pi$, a phase shift covering $2\pi$ can be obtained when the fundamental compressional mode of the pillar is superposed with one of the bending modes. Since each resonant pillar of the metasurface acts as a secondary emitter source of waves with a different phase shift, the metasurface can be designed with a suitable arrangement of pillars such that all the transmitted waves interfere constructively

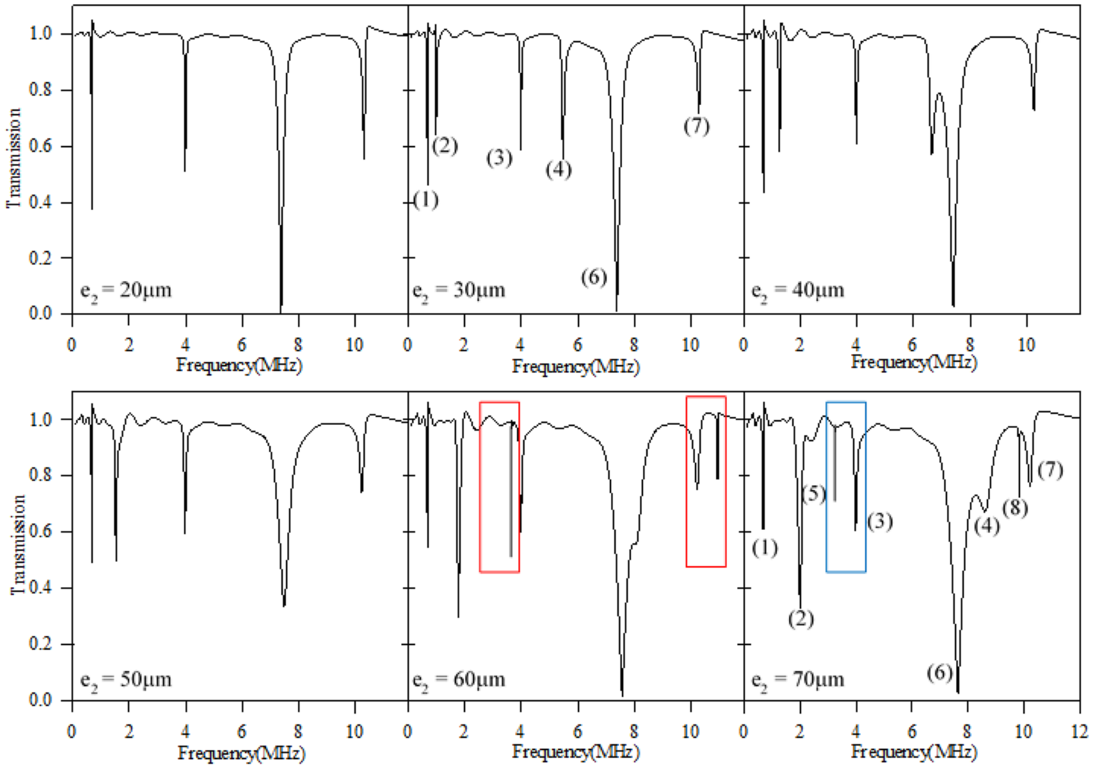

**FIG. 4.** Transmission through a line of elliptical pillars whose major axis $e_2$ is rotated with respect to the direction of propagation of the incident wave with an angle $\varphi = 45°$. Each curve is associated with a different value of $e_2$, ranging from $e_2 = 20$ µm, corresponding to the cylindrical pillar, to $e_2 = 70$ µm, in steps of 10 µm.

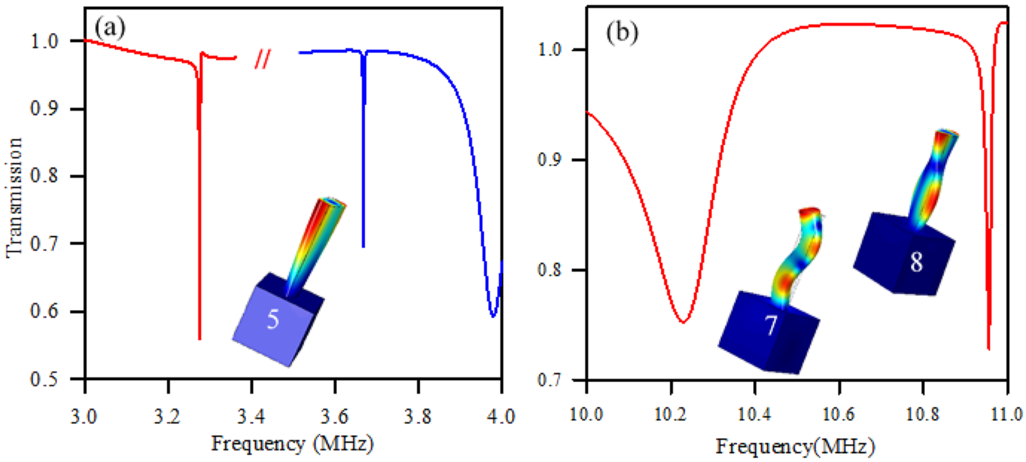

**FIG. 5.** Zoom of the colored boxes in Fig. 4 shows: (a) first-order torsional mode (5) for $e_2 = 60$ µm (red solid line) and $e_2 = 70$ µm (blue solid line), and (b) third-order bending mode (7) and second-order torsional mode (8) for $e_2 = 60$ µm. The insets represent the corresponding eigenmodes.

and create a focal point on the plate based on their relative path difference.

One can note that in Fig. 6(b), a second crossing occurs between modes 7 and 8, at $e_2 = 68$ $\mu$m, which could potentially be used to make the focusing gradient metasurface. However, branch 8, associated with the second-order torsional mode, has a very narrow signature in the transmission [Fig. 5(a)] that makes the phase variation too sharp on a small frequency range and may not be

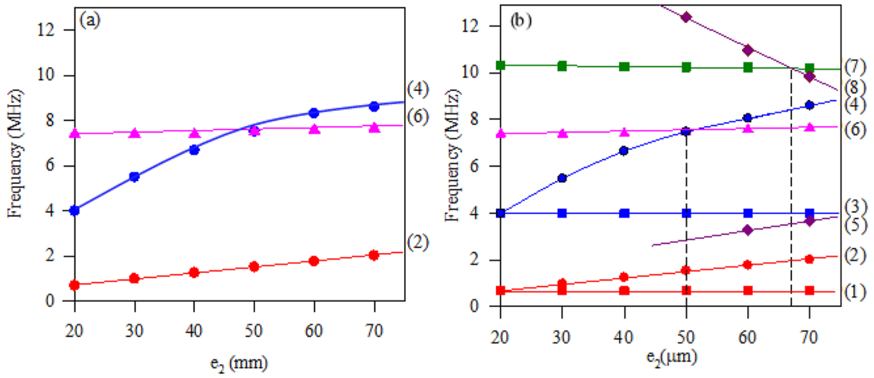

**FIG. 6.** Resonance frequencies of the elliptic pillar in the transmission spectra for values of the ellipticity parameter range from $e_2$ = 20 μm (corresponding to a cylindrical pillar) to $e_2$ = 70 μm. (a) $\varphi$ = 0° and (b) $\varphi$ = 45°. In both cases, the second bending mode (4) and the first compressional mode (6) overlap at $f$ = 7.48 MHz when $e_2$ = 50 μm.

suitable for the design of the metasurface. Therefore, in the next section, the focusing functionality is demonstrated for $\varphi = 0°$ around $e_2 = 50\ \mu$m, for which the bending and compressional modes overlap in a large frequency range.

## IV. SUBWAVELENGTH FOCUSING

Thanks to the ability of the pillars to generate transmitted waves with a full $2\pi$ phase range of the phase shift and sufficiently high-transmission amplitude, we can design a gradient-phase line of pillars to realize anomalous transmitted wave fronts based on the generalized Snell law,

$$n_1 \sin \theta_1 - n_2 \sin \theta_2 = \frac{\lambda}{2\pi}\frac{d\Phi(y)}{dy}. \qquad (1)$$

We apply this relationship to create a discrete distribution of resonators associated with a discrete distribution of phase. As an illustration of anomalous transmission, we present a structure allowing the focus of a transmitted Lamb wave $A_0$ at any point of the surface M($x_0$, $y_0$). To do that, a line of 31 elliptic pillars spaced by 100 μm is arranged along the $y$ direction perpendicular to the wave propagation. The phase profile $\Phi(y)$ along this direction is determined according to the relation,

$$\Phi(y) - \Phi(y_0) = \frac{2\pi}{\lambda}\left(\sqrt{(y-y_0)^2 + x_0^2} - \sqrt{y_0^2 + x_0^2}\right). \qquad (2)$$

At frequency $f$ = 7.48 MHz, where the first compressional mode and the second bending mode overlap, the wavelength of the incident $A_0$ Lamb wave is equal to $\lambda$ = 445 μm (see red line in Fig. 1, where $k_x.a$ = 2.11 for the $A_0$ mode at $f$ = 7.48 MHz). The phase of the central pillar ($y$ = 0) is set to $-\pi$, corresponding to the strongest resonant status. We first present the focusing effect at a point M whose coordinates are $(x_0, y_0) = (\lambda, 0)$. For this focal point, the discrete theoretical phases $\Phi(y)$ of the 30 other pillars of the line are calculated from Eq. (2) as a function of their positions $y$ [Fig. 7(a)] and compared to the numerical calculation of the phase as a function of $e_2$ [Fig. 7(b)]. In Fig. 7(b), the solid black line depicts the phase response of a pillar with varying ellipticity ranging from 15 to 200 $\mu$m at a frequency of 7.48 MHz. For each position $y$ of the pillar on the metasurface, the corresponding phase value is determined along the red dashed lines shown in Fig. 7(a). For instance, at the position $y = 5\ \mu$m, the phase is zero [Fig. 7(a)], which, according to Fig. 7(b), corresponds to a value of $e_2 = 172\ \mu$m. The evolution of the ellipticity parameter $e_2$ is represented as a function of the pillars' positions in the top panel in Fig. 7(a), covering the phase variation of $2\pi$ for the set of 31 pillars.

Figure 8 shows the out-of-plane displacement ($u_z$) field distribution and the transmitted amplitude around the focal point (i.e., along the white vertical line), which shows a significant focusing effect with a sub-wavelength full width at half maximum (FWHM) of $\lambda/3$. It should be noted that this sub-wavelength focusing can be further improved by increasing the number of pillars and, hence, the lateral length of the metasurface. The right panel in Fig. 8 shows the intensity of the field along the red line, normalized to the intensity of the field crossing the plate without the metasurface. One can see that the intensity at the focal point is 3.7 times higher than that of the incident field, presenting a compelling opportunity for energy harvesting applications. Moreover, we have checked that incorporating a disorder in the value of $e_2$ with a fluctuation of +/− 1 $\mu$m resulted in a 15% reduction of the intensity at the focal point. This provides an acceptable range of tolerance in the microfabrication process.

As a further example of the metasurface's ability to manipulate transmitted waves, we have simulated the focusing effect of a row of 31 pillars. The procedure to design the metasurface is the same as that described above: once the position $y$ of each pillar has been fixed and the position of the focusing spot $(x_0, y_0)$ chosen, the value of the phase $\Phi(y)$ is calculated from Eq. (2), and the value of the ellipticity parameter $e_2$ is thus determined from the calculated variation of $e_2$ vs $\Phi$. The results obtained for two focusing spots with coordinates $(2\lambda, 0)$ and $(\lambda, \lambda)$ are reported in Fig. 9.

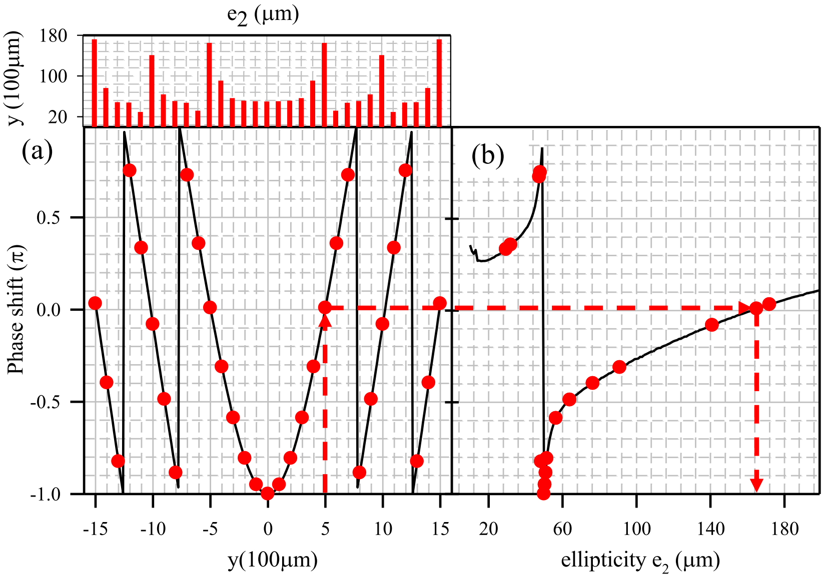

**FIG. 7.** (a) Theoretical phase profile (solid line) for focusing at the ($\lambda$, 0) coordinate point, with $\Phi(y_0 = 0) = -\pi$ [see Eq. (2)] and discrete phases of the 31 selected pillars for the metasurface (red dots). (b) Variation of transmitted phase (black solid curve) in a periodic array of 31 pillars as a function of ellipticity $e_2$, for a constant value $e_1 = 20$ μm at the frequency $f = 7.48$ MHz. The values of $e_2$ used in the metasurface design (red dots) are determined from (a). Top in Fig. 7(a): Representation of the ellipticity parameter $e_2$ as a function of the position of the pillars along $y$.

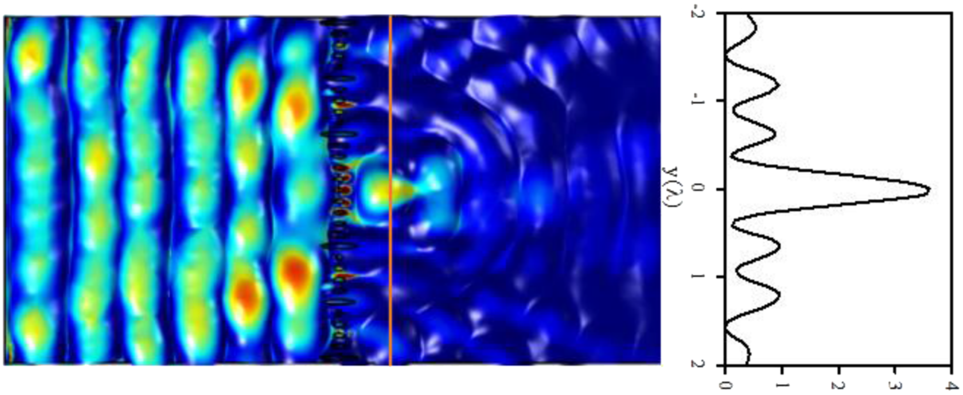

**FIG. 8.**. *Left*: Illustration of the focusing effect of an incident plane-wave ($\lambda = 445$ μm) by an array of 31 elliptic shaped pillars. The focal point is targeted at F = $\lambda$. *Right*: Intensity $|u_z^2|$ along the $y$ axis (red line) crossing the focusing spot, normalized to the reference $|u_{zp}^2|$ along the same line without the metasurface.

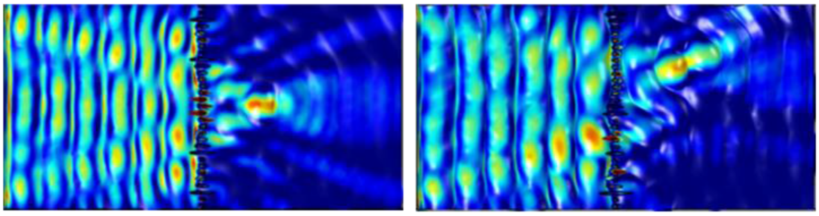

**FIG. 9.** Focusing effect at two different points M($x_0$, $y_0$) of the plate. Left panel: M(2$\lambda$, 0) and right panel: M($\lambda$, $\lambda$), where $\lambda = 445$ μm.

## V. CONCLUSIONS AND FURTHER DEVELOPMENTS

In this paper, the study of different elliptical pillar resonance modes has enabled us to propose a type of elastic metasurface consisting of a line of resonant pillars with constant height and variable ellipticity. The pillars have been arranged on a homogeneous plate. Our design can provide full phase range manipulation and high transmission. The $2\pi$ variation of the phase was made possible by superimposing, for a given value of ellipticity, a bending mode and a compressional mode. A particularly striking advantage of this structure is that, due to its constant height, it is likely that it can be relatively easily fabricated at the micro- and even nano-scale using current nanofabrication techniques, i.e., metal-assisted chemical etching (MACE)[28] or deep reactive ion etching (DRIE),[29] which allow for pillars with very high aspect ratios. Moreover, this structure can be adapted to the wavelength of the incident wave by varying the height of the pillars and determining a new value of $e_2$ related to the two modes to be superimposed at the frequency of the incident wave. We have demonstrated the possibility of precisely selecting the focus points by adjusting the ellipticity of the pillars. This capability not only enhances our control over the focus point but also facilitates a significant concentration of energy, presenting valuable applications in integrated devices, for instance in electro-mechanic designs used in optomechanical applications. To illustrate this, we refer to our recent paper,[30] where an acoustic wave was injected into an optomechanical cavity inside a nanobeam by means of surface acoustic waves generated in front of the nanobeam by a set of interdigital transducers (IDTs). Incorporating a metasurface in front of the IDTs offers the opportunity to focus the energy directly inside a connected, freestanding nanobeam. We have also emphasized the possibility of activating torsional modes by changing the orientation of the pillars with respect to the direction of propagation of the incident wave. These modes can be superimposed with compression and bending modes, but the phase shift analysis for the associated $e_2$ values shows phase variations of $\pi$ only, so they cannot be used to create a wave-focusing metasurface. Nevertheless, these torsional modes are characterized by very high-quality factors that can make them valuable in high-sensitivity sensors or as very selective filters.

## ACKNOWLEDGMENTS

L.C., R.A.-G., C.C., M.M., Y.P., and B.D.-R. thank the MAGNIFIC, funded by the European Union's Horizon Europe research and innovation program under grant agreement No. 101091968. A.G. and G.L. thank the Chist-ERA Call 2021, funded by national agencies AEI (Spain), ANR (France), and AKA (Finland) under Grant Agreement No. CHIST-ERA-20-NOEMS-003.

## AUTHOR DECLARATIONS

### Conflict of Interest

The authors have no conflicts to disclose.

### Author Contributions

**L. Carpentier**: Conceptualization (equal); Data curation (equal); Formal analysis (equal); Investigation (equal); Methodology (equal); Writing – original draft (equal); Writing – review & editing (equal). **A. Gueddida**: Formal analysis (equal); Investigation (equal); Methodology (equal); Validation (equal). **G. Lévêque**: Formal analysis (equal); Methodology (equal); Supervision (equal); Validation (equal). **R. Alcorta-Galvan**: Validation (equal); Visualization (equal); Writing – review & editing (equal). **C. Croënne**: Validation (equal); Visualization (equal); Writing – review & editing (equal). **M. Miniaci**: Validation (equal); Visualization (equal); Writing – review & editing (equal). **B. Djafari-Rouhani**: Conceptualization (equal); Formal analysis (equal); Supervision (equal); Validation (equal); Visualization (equal); Writing – review & editing (equal). **Y. Pennec**: Conceptualization (equal); Data curation (equal); Funding acquisition (equal); Supervision (equal); Validation (equal); Writing – review & editing (equal).

## DATA AVAILABILITY

The data that support the findings of this study are available from the corresponding author upon reasonable request.

## REFERENCES

[1] F. Ding, A. Pors, and S. I. Bozhevolnyi, "Gradient metasurfaces: A review of fundamentals and applications," Rep. Prog. Phys. **81**, 026401 (2017).

[2] N. Yu and F. Capasso, "Flat optics with designer metasurfaces," Nat. Mater. **13**, 139 (2014).

[3] D. Lin, P. Fan, E. Hasman, and M. L. Brongersma, "Dielectric gradient metasurface optical elements," Science **345**(6194), 298–302 (2014).

[4] A. Zhan, S. Colburn, R. Trivedi, T. K. Fryett, C. M. Dodson, and A. Majumdar, "Low-contrast dielectric metasurface optics," ACS Photonics **3**(2), 209–214 (2016).

[5] S. A. Cummer, J. Christensen, and A. Alù, "Controlling sound with acoustic metamaterials," Nat. Rev. Mater. **1**, 16001 (2016).

[6] B. Assouar, B. Liang, Y. Wu, Y. Li, J. C. Cheng, and Y. Jing, "Acoustic metasurfaces," Nat. Rev. Mater. **3**(12), 460–472 (2018).

[7] G. Ma and P. Sheng, "Acoustic metamaterials: From local resonances to broad horizons," Sci. Adv. **2**(2), e1501595 (2016).

[8] A. L. Chen, Y. S. Wang, Y. F. Wang, H. T. Zhou, and S. M. Yuan, "Design of acoustic/elastic phase gradient metasurfaces: Principles, functional elements, tunability, and coding," Appl. Mech. Rev. **74**, 020801 (2022).

[9] X. Wang, R. Dong, Y. Li, and Y. Jing, "Non-local and non-Hermitian acoustic metasurfaces," Rep. Prog. Phys. **86**, 116501 (2023).

[10] Y. Wu, Y. Lai, and Z. Q. Zhang, "Elastic metamaterials with simultaneously negative effective shear modulus and mass density," Phys. Rev. Lett. **107**(10), 105506 (2011).

[11] Y. Jin, Y. Pennec, B. Bonello, H. Honarvar, L. Dobrzynski, B. Djafari-Rouhani, and M. I. Hussein, "Physics of surface vibrational resonances: Pillared phononic crystals, metamaterials, and metasurfaces," Rep. Prog. Phys. **84**, 086502 (2021).

[12] H. Huang, J. Chen, and S. Huo, "Recent advances in topological elastic metamaterials," J. Phys.: Condens. Matter **33**(50), 503002 (2021).

[13] M. Oudich, N. J. Gerard, Y. Deng, and Y. Jing, "Tailoring structure-Borne sound through bandgap engineering in phononic crystals and metamaterials: A comprehensive review," Adv. Funct. Mater. **33**(2), 2206309 (2023).

[14] A. O. Krushynska, D. Torrent, A. M. Aragón, R. Ardito, O. R. Bilal, B. Bonello, F. Bosia *et al.*, "Emerging topics in and elastic, acoustic, and mechanical metamaterials: An overview," Nanophotonics **12**(4), 659–686 (2023).

[15] L. Cao, Z. Yang, Y. Xu, and B. Assouar, "Deflecting flexural wave with high transmission by using pillared elastic metasurface," Smart Mater. Struct. **27**(7), 075051 (2018).

[16] H. Zhu and F. Semperlotti, "Anomalous refraction of acoustic guided waves in solids with geometrically tapered metasurfaces," Phys. Rev. Lett. **117**(3), 034302 (2016).

[17] Y. Xie, W. Wang, H. Chen, A. Konneker, B. I. Popa, and S. A. Cummer, "Wavefront modulation and subwavelength diffractive acoustics with an acoustic metasurface," Nat. Commun. **5**(1), 5553 (2014).

[18] J. Zhang, X. Su, Y. Pennec, Y. Jing, X. Liu, and N. Hu, "Wavefront steering of elastic shear vertical waves in solids via a composite-plate-based metasurface," J. Appl. Phys. **124**(16), 164505 (2018).

[19] M. Rupin, S. Catheline, and P. Roux, "Super-resolution experiments on lamb waves using a single emitter," Appl. Phys. Lett. **106**, 024103 (2015).

[20] S. Guenneau, A. Movchan, G. Pétursson, and S. Anantha Ramakrishna, "Acoustic metamaterials for sound focusing and confinement," New J. Phys. **9**(11), 399 (2007).

[21] R. Sabat, Y. Pennec, G. Lévêque, D. Torrent, C. Ding, and B. Djafari-Rouhani, "Single and coupled Helmholtz resonators for low frequency sound manipulation," J. Appl. Phys. **132**(6), 064505 (2022).

[22] G. Ma, M. Yang, S. Xiao, Z. Yang, and P. Sheng, "Acoustic metasurface with hybrid resonances," Nat. Mater. **13**(9), 873–878 (2014).

[23] Y. Pennec, B. Djafari-Rouhani, H. Larabi, J. O. Vasseur, and A. C. Hladky-Hennion, "Low-frequency gaps in a phononic crystal constituted of cylindrical dots deposited on a thin homogeneous plate," Phys. Rev. B **78**(10), 104105 (2008).

[24] P. Celli, B. Yousefzadeh, C. Daraio, and S. Gonella, "Bandgap widening by disorder in rainbow metamaterials," Appl. Phys. Lett. **114**(9), 091903 (2019).

[25] X. Wu, Z. Wen, Y. Jin, T. Rabczuk, X. Zhuang, and B. Djafari-Rouhani, "Broadband Rayleigh wave attenuation by gradient metamaterials," Int. J. Mech. Sci. **205**, 106592 (2021).

[26] W. Wang, B. Bonello, B. Djafari-Rouhani, Y. Pennec, and J. Zhao, "Elastic stubbed metamaterial plate with torsional resonances," Ultrasonics **106**, 106142 (2020).

[27] Y. Jin, W. Wang, A. Khelif, and B. Djafari-Rouhani, "Elastic metasurfaces for deep and robust subwavelength focusing and imaging," Phys. Rev. Appl. **15**, 024005 (2021).

[28] K. Yamada, M. Yamada, H. Maki, and K. M. Itoh, "Fabrication of arrays of tapered silicon micro-/nano-pillars by metal-assisted chemical etching and anisotropic wet etching," Nanotechnology **29**, 28LT01 (2018).

[29] C. H. Choi and C. J. Kim, "Fabrication of a dense array of tall nanostructures over a large sample area with sidewall profile and tip sharpness control," Nanotechnology **17**, 5326 (2006).

[30] A. V. Korovin, Y. Pennec, M. Stocchi, D. Mencarelli, L. Pierantoni, T. Makkonen *et al.*, "Conversion between surface acoustic waves and guided modes of a quasi-periodic structured nanobeam," J. Phys. D: Appl. Phys. **52**(32), 32LT01 (2019).